



ARHGAP1 Transported with Influenza Viral Genome Ensures Integrity of Viral Particle Surface through Efficient Budozone Formation

 Takahiro Kuroki,^a Tomohisa Hatta,^{b,c} Tohru Natsume,^{b,c} Nobuaki Sakai,^d Akira Yagi,^e Kohsuke Kato,^{a,f} Kyosuke Nagata,^f Atsushi Kawaguchi^{a,f,g,h}

^aGraduate School of Comprehensive Human Sciences, University of Tsukuba, Tsukuba, Japan

^bRobotic Biology Institute Inc., Tokyo, Japan

^cMolecular Profiling Research Center, National Institute for Advanced Industrial Science and Technology, Tokyo, Japan

^dDepartment of Cell Physiology, Faculty of Medicine and Graduate School of Medicine, Hokkaido University, Sapporo, Japan

^eR&D Group, Olympus Corporation, Hachioji, Japan

^fDepartment of Infection Biology, Faculty of Medicine, University of Tsukuba, Tsukuba, Japan

^gTransborder Medical Research Center, University of Tsukuba, Tsukuba, Japan

^hMicrobiology Research Center for Sustainability, University of Tsukuba, Tsukuba, Japan

ABSTRACT Influenza viral particles are assembled at the plasma membrane concomitantly with Rab11a-mediated endocytic transport of viral ribonucleoprotein complexes (vRNPs). The mechanism of spatiotemporal regulation of viral budozone formation and its regulatory molecules on the endocytic vesicles remain unclear. Here, we performed a proximity-based proteomics approach for Rab11a and found that ARHGAP1, a Rho GTPase-activating protein, is transported through the Rab11a-mediated apical transport of vRNP. ARHGAP1 stabilized actin filaments in infected cells for the lateral clustering of hemagglutinin (HA) molecules, a viral surface membrane protein, to the budozone. Disruption of the HA clustering results in the production of virions with low HA content, and such virions were less resistant to protease and had enhanced antigenicity, presumably because reduced clustering of viral membrane proteins exposes hidden surfaces. Collectively, these results demonstrate that Rab11a-mediated endocytic transport of ARHGAP1 with vRNPs stimulates budozone formation to ensure the integrity of virion surface required for viral survival.

IMPORTANCE The endocytic transport of the influenza viral genome triggers the clustering of viral membrane proteins at the plasma membrane to form the viral budozone. However, host factors that promote viral budozone formation in concert with viral genome transport have not been identified. Here, we found that ARHGAP1, a negative regulator of the Rho family protein, is transported with the viral genome and stabilizes actin filaments to promote budozone formation. We have shown that ARHGAP1-mediated efficient formation of viral budozone was crucial for the clustering of viral HA protein to the progeny viral particles. The clustering of HA proteins on the virions is responsible for the structural integrity of the viral particles, which promotes viral stability and viral immune evasion. This study highlights the molecular mechanism that works in concert with viral genome packaging to ensure the structural integrity of viral particles.

KEYWORDS actin filament, influenza virus, recycling endosome, viral assembly

Influenza A virus (IAV) has two major outer spike proteins, hemagglutinin (HA) and neuraminidase (NA), on its viral particles. HA is the major antigen for neutralizing antibodies and causes antigenic drift of the virus by human herd immunity, which is mostly directed against the globular head domain of HA densely packed on the viral

Editor Matthew S. Miller, McMaster University

Copyright © 2022 Kuroki et al. This is an open-access article distributed under the terms of the [Creative Commons Attribution 4.0 International license](https://creativecommons.org/licenses/by/4.0/).

Address correspondence to Atsushi Kawaguchi, ats-kawaguchi@md.tsukuba.ac.jp.

The authors declare no conflict of interest.

Received 13 March 2022

Accepted 7 April 2022

Published 27 April 2022

particles (1–3). Little is yet known about the mechanism of the well-organized recruitment of viral spike proteins to the viral budding site to guarantee the structural integrity of the viral particles.

The IAV genome consists of eight single-stranded RNA segments of negative polarity. The viral genome exists as viral ribonucleoprotein complexes (vRNPs) by interacting with viral RNA-dependent RNA polymerases and nucleoprotein (NP). After nuclear transport of replicated vRNPs, the vRNPs are transported to the plasma membrane through Rab11a-positive recycling endosomes along microtubules for viral particle formation (4–7). The viral budding site, called the budozone, serves as a platform to concentrate the viral components at the plasma membrane. The assembly of the budozone is mediated by the formation of lipid rafts, which are membrane microdomains enriched in cholesterol/sphingolipids (8–10). HA and NA are intrinsically targeted to cholesterol-rich small lipid rafts and accumulate to the budozone through the clustering of small lipid rafts (11, 12). In contrast, viral protein M2 localizes to the boundary between the budozone and the bulk plasma membrane owing to its relatively short transmembrane domain, which prevents the insertion of M2 into ordered and tightly packed lipid rafts (13, 14). M2 has been proposed to mediate a viral membrane scission from the plasma membrane (15). Viral matrix protein M1 serves as an inner envelope-associated scaffold by interacting with both vRNPs and the cytoplasmic tails of HA and NA (16, 17).

Membrane trafficking mediated by Rab proteins is a major system to regulate the transport of cellular constituents between membrane organelles (18, 19). Rab proteins are small GTPases that are activated by a guanine nucleotide exchange reaction from GDP to GTP and bind to Rab effectors (20, 21). Through a recruitment of specific Rab effectors, Rab proteins function as molecular switches to deliver cargoes to their destinations by controlling the formation, motility, and fusion of endocytic vesicles (22). Endocytic recycling is carried out in either a direct manner, termed “fast recycling,” or “slow recycling,” that is mediated by endocytic recycling compartments (ERCs), which are a collection of tubular organelles around the microtubule-organizing center (MTOC) (23, 24). Rab11a-positive recycling endosomes (Rab11a REs) egress from ERCs and regulate the slow recycling pathway. Activated Rab11a interacts with its effector Rab11 family-interacting proteins (Rab11-FIPs). Rab11-FIPs are classified into two classes: class I (FIP1/RCP, FIP2, and FIP5/Rip11) and class II (FIP3 and FIP4). The Rab11-FIPs contain a highly conserved C-terminal Rab11-binding domain (RBD) and either a C2 domain (class I) or an EF-hand domain (class II) in the N terminus. FIPs regulate the dynamics of REs by bridging Rab11a and molecular motors (25). FIP2 and FIP5 interact with MyoVb and Kif3, respectively (26, 27), whereas FIP3 binds to dynein through Dyncli1 (28). Although the dynamics of endocytic transport mediated by REs are activated in infected cells (29), the function of FIPs in vRNP transport remains controversial. It has been reported that the overexpression of FIP RBDs dominant negatively disrupted the vRNP accumulation in ERCs, suggesting that the apical transport of vRNPs is mediated by FIPs (5). On the other hand, it has also been reported that vRNP binding to REs competes for the interaction of FIPs with Rab11a (29).

Using proximity-dependent biotin identification (BioID) screening, we identified cellular proteins involved in the endocytic transport and the organization of the actin cytoskeleton, including FIP2, FIP5, and ARHGAP1, a GTPase-activating protein (GAP) for the Rho GTPase family, as Rab11a-binding proteins in IAV-infected cells. ARHGAP1 was colocalized with vRNP in Rab11a REs, and their endocytic transport to the plasma membrane was dependent on FIP2 and FIP5. The vRNP transport promotes the clustering of HA to the viral budozone through the actin stabilization by ARHGAP1. We also found that knockdown (KD) of ARHGAP1 or FIP5 reduced viral titers and formed defective viral particles with low HA content that were less resistant to protease treatment and had enhanced antigenic potential. Collectively, we propose that the efficient budozone formation mediated by the Rab11a-ARHGAP1 pathway not only promotes the virus production but also guarantees the integrity of viral particle surface required for survival in the host environment.

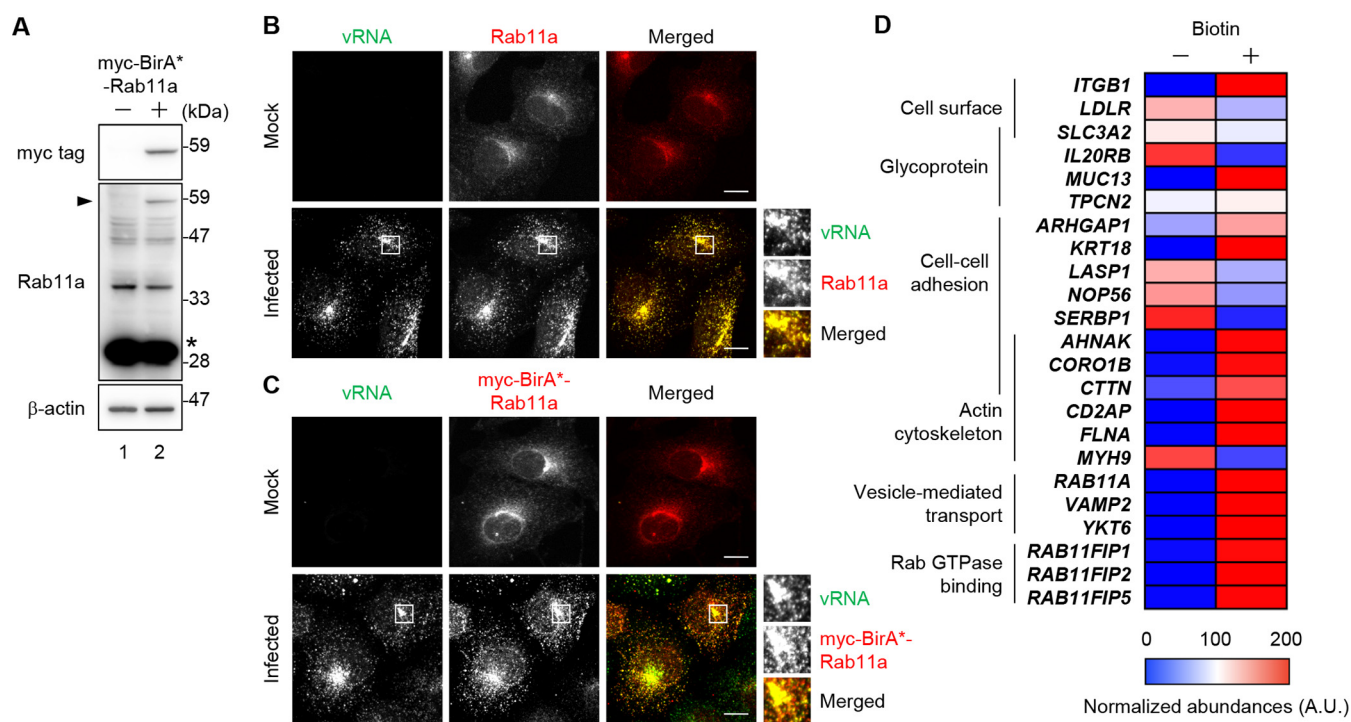


FIG 1 Identification of Rab11a-interacting proteins in IAV-infected cells. (A) Expression level of myc-BirA^{*}-Rab11a. The cell lysates were obtained from A549 cells (lane 1) or myc-BirA^{*}-Rab11a A549 cells (lane 2) and subjected to Western blot analyses with anti-myc tag, anti-Rab11a, and anti- β -actin antibodies. The asterisk and arrowhead indicate endogenous Rab11a and myc-BirA^{*}-Rab11a, respectively. (B and C) At 4 h postinfection, A549 cells (B) and myc-BirA^{*}-Rab11a A549 cells (C) were subjected to indirect immunofluorescence assays with anti-Rab11a (red in panel B) or anti-myc tag (red in panel C) antibodies, followed by FISH assays to detect seg7 vRNA (green). The enlarged panels show ERCs. Representative images from three independent experiments are shown. Scale bars, 10 μ m. (D) Gene ontology analysis of Rab11a-interacting proteins in IAV-infected A549 cells was carried out using the DAVID database. The heatmap shows the normalized peptide abundance of identified proteins in LC-MS with or without the addition of biotin.

RESULTS

FIP2- and FIP5-positive recycling endosomes regulate anterograde transport of vRNPs. To identify the effector molecules that regulate the dynamics of Rab11a REs in infected cells, we carried out proximity-dependent biotin identification (BioID) assay with A549 cells stably expressing myc-tagged R118G-mutated BirA (BirA^{*})-fused Rab11a (Text S1). BirA is a bacterial biotin ligase that recognizes a specific amino acid sequence and links biotin to a lysine residue in the peptide by forming biotinoyl-5'-AMP (30). The promiscuous mutant BirA^{*} has a lower affinity than wild-type BirA for biotinoyl-5'-AMP; thus, the active form of biotin transfers to lysine residues of proteins, which locate within a radius of 10 nm to a protein of interest fused to BirA^{*} (31). The expression level of myc-BirA^{*}-Rab11a (Fig. 1A, arrowhead) was less than that of endogenous Rab11a (Fig. 1A, asterisk). At 4 h postinfection, myc-BirA^{*}-Rab11a was colocalized with the viral genome in the ERCs at the perinuclear regions as endogenous Rab11a was (Fig. 1B and C). The myc-BirA^{*}-Rab11a A549 cells were infected with IAV at a multiplicity of infection (MOI) of 10 in the absence or presence of 50 μ M biotin. At 8 h postinfection, the cell lysates were subjected to affinity purification with streptavidin beads. The purified biotinylated proteins were analyzed by liquid chromatography-mass spectrometry (LC-MS), and the identified proteins related to the cell surface, glycoproteins, cell-cell adhesion, actin cytoskeleton, vesicle-mediated transport, and Rab GTPase binding were shown (Fig. 1D and Table S1 in the supplemental material). We found that Rab11a interacts with class I Rab11-FIPs (FIP1, FIP2, and FIP5), but not class II Rab11-FIPs (FIP3 and FIP4), in infected cells (Fig. 1D). It was also observed that ARHGAP1, which functions as a GAP mainly for Cdc42 and RhoA, interacted with Rab11a in infected cells (Fig. 1D). It is reported that ARHGAP1 controls the assembly and disassembly of the actin filaments for transferrin uptake by regulating Rho GTPases (32–34).

To identify class I FIPs that are involved in the transport of vRNPs, we next examined the intracellular localization of viral RNA (vRNA) with FIP1C, FIP2, or FIP5 in infected A549

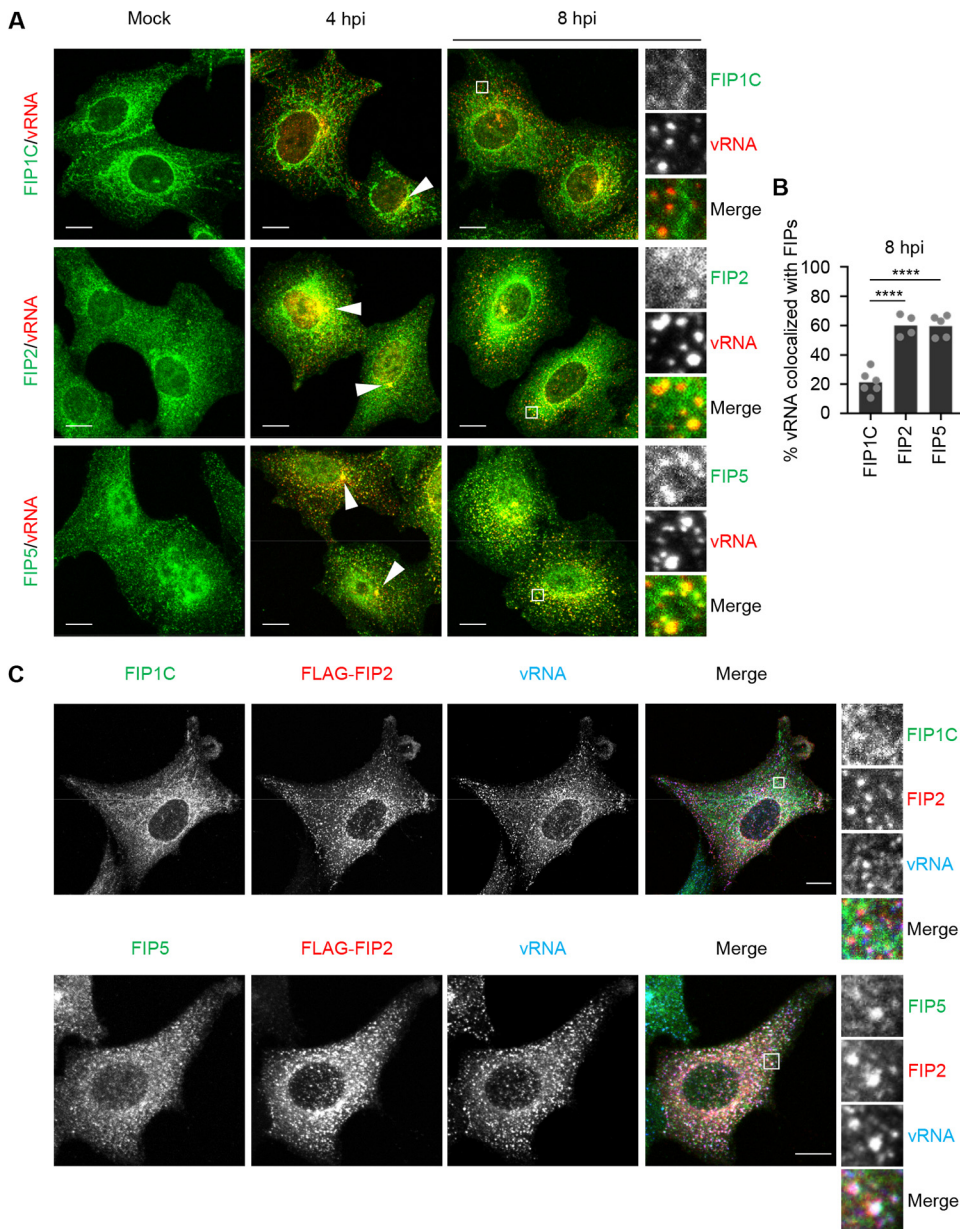


FIG 2 vRNPs colocalize with FIP2 and FIP5 but not with FIP1C. (A) A549 cells were infected with PR8 virus at an MOI of 10. At 4 and 8 h postinfection, the cells were subjected to indirect immunofluorescence assays with antibodies against class I FIPs (green), followed by FISH assays to detect seg7 vRNA (red). Arrowheads indicate ERCs. (B) Percentage of vRNA colocalized with FIPs in the cytoplasmic region of panel A at 8 h postinfection, excluding the region around ERC, was quantified using Imaris software ($n = 4$ to 6 cells/group). ****, $P < 0.0001$; one-way ANOVA with Tukey's test. (C) At 24 h posttransfection of FLAG-FIP2 (red), A549 cells were infected with PR8 virus at an MOI of 10. At 8 h postinfection, FIP1B (green, top), FIP5 (green, bottom), and seg7 vRNA (blue) were visualized by indirect immunofluorescence assays and FISH assays, respectively. Representative images from three independent experiments are shown. Scale bars, 10 μm (A and C).

cells by indirect immunofluorescence assays and fluorescence *in situ* hybridization (FISH) assays (Fig. 2A). At 4 h postinfection, vRNA was colocalized with class I FIPs in the ERCs (Fig. 2A, arrowheads). However, upon the relocation of vRNA in punctate cytoplasmic structures for the apical transport at 8 h postinfection, the dispersed vRNA was colocalized with FIP2 and FIP5 only, but not with FIP1C (Fig. 2A and B). Furthermore, transiently expressed FLAG-FIP2 was colocalized with FIP5, but not with FIP1C (Fig. 2C).

At 48 h posttransfection of scrambled small interfering RNA (siRNA) (siCtrl) or siRNA for *RAB11FIP2* (siFIP2) or *RAB11FIP5* (siFIP5), the expression levels of FIP2 and FIP5 in

the KD cells had decreased to less than 10% of that in the control cells, respectively (Fig. S1A and B). Note that the expression level of NP was not changed by FIP KD (Fig. S1C). We found that the extent of vRNP accumulation at the ERCs in FIP2 KD or FIP5 KD cells was comparable to that in the control cells at 4 h postinfection (Fig. 3A and B). However, vRNPs remained in the ERCs even at 8 h postinfection in FIP2 KD or FIP5 KD cells (Fig. 3A and B and Fig. S2A and B), suggesting that FIP2 and FIP5 cooperatively regulate the apical transport of vRNPs by Rab11a REs emanated from ERCs. We also found that FLAG-ARHGAP1 localized with vRNA in the ERCs at 4 h postinfection (Fig. 3C, arrowheads). Furthermore, at 8 h postinfection, FLAG-ARHGAP1 signals translocated to the punctate cytoplasmic structures with vRNA in an FIP5-dependent manner (Fig. 3C, arrows, and Fig. 3D), indicating that ARHGAP1 is transported to the plasma membrane with vRNA through Rab11a REs.

Formation of the budozone requires actin filaments. The assembly and membrane protrusion of the viral budozone are coupled with the clustering of lipid rafts in which viral membrane proteins are embedded (35, 36). Thus, we examined the dynamics of budozone formation by a high-speed atomic force/fluorescence microscopy imaging system (BIXAM). At 1 h posttransfection of HA-Venus and M2-mCherry, the cells were infected with IAV at an MOI of 10 for 12 h. The budozone-like protrusions were approximately 500 nm in diameter as previously observed by transmission electron microscopy (TEM) imaging (Fig. 4A, arrowheads) (3, 37). Further, the protrusions colocalized with HA-Venus and M2-mCherry were persistently observed over a few minutes (Fig. 4B, arrowheads). It was clearly distinct from membrane ruffles, which were less than 400 nm in diameter and disappeared within tens of seconds (Fig. 4A, arrows). In the budozone-like protrusions, M2-mCherry was surrounded by HA-Venus in a ringlike pattern (Fig. 4B to D). This is in good agreement with the fact that M2 mediates the pinching off of virus particles from the plasma membrane (15). In contrast, a mutant HA harboring alanine substitutions (I532A, Y533A, and S534A) in the cholesterol-binding domain, referred to as nonraft HA (38, 39), hardly colocalized with M2 in the protruding structures (Fig. 4E to G). Although we have not excluded the possibility that nonraft HA is defective in the interaction with other structural proteins such as M1 and M2, it is possible that the accumulation of HA in the viral budozone is mediated by lipid rafts at the plasma membrane through the binding of HA to cholesterol.

It is proposed that the formation of lipid rafts requires the lateral mobility of membrane molecules at the plasma membrane through cortical actin filaments (40, 41). We found that actin filaments visualized by expressing Lifeact-TagGFP2 associate with the budozone-like protrusions (Fig. 5A, arrowheads). Further, the budozone was rapidly made to disappear by addition of 50 μ M cytochalasin D (CytoD), a potent actin polymerization inhibitor (Fig. 5B, arrowheads). These results indicated that actin filaments function as a scaffold to assemble the viral budozone at the plasma membrane. We also tested the dynamics of actin filaments in infected cells expressing Lifeact-TagGFP2 by fluorescence recovery after photobleaching (FRAP) assays. The mean half-recovery time of Lifeact-TagGFP2 was 5.60 s for infected cells, but 3.97 s for uninfected cells (Fig. 5C and D and Fig. S2A), indicating that actin filaments are relatively stabilized by IAV infection. We also examined the actin dynamics by FRAP assays in FIP5 KD (siFIP5) or ARHGAP1 KD cells (siARHGAP1). The expression levels of ARHGAP1 in the KD cells decreased to about 20% of those in the control cells (Fig. S3A). The delay of the mean half-recovery time of Lifeact-TagGFP2 upon IAV infection was not observed in FIP5 KD or ARHGAP1 KD cells (Fig. 5C and D and Fig. S3B to D). However, this was not the case for FIP1 KD cells (Fig. S4A to C). It is likely that actin filaments are stabilized by ARHGAP1 transported to the plasma membrane through FIP5-regulated REs in infected cells.

Efficient budozone formation confers protease resistance and reduced antigenicity to the viral particles. We next examined the formation of the viral budozone in FIP5 KD and ARHGAP1 KD cells by *in situ* proximity ligation assays (PLAs) to detect the close proximity between HA and M2. The number of PLA signals between HA and M2

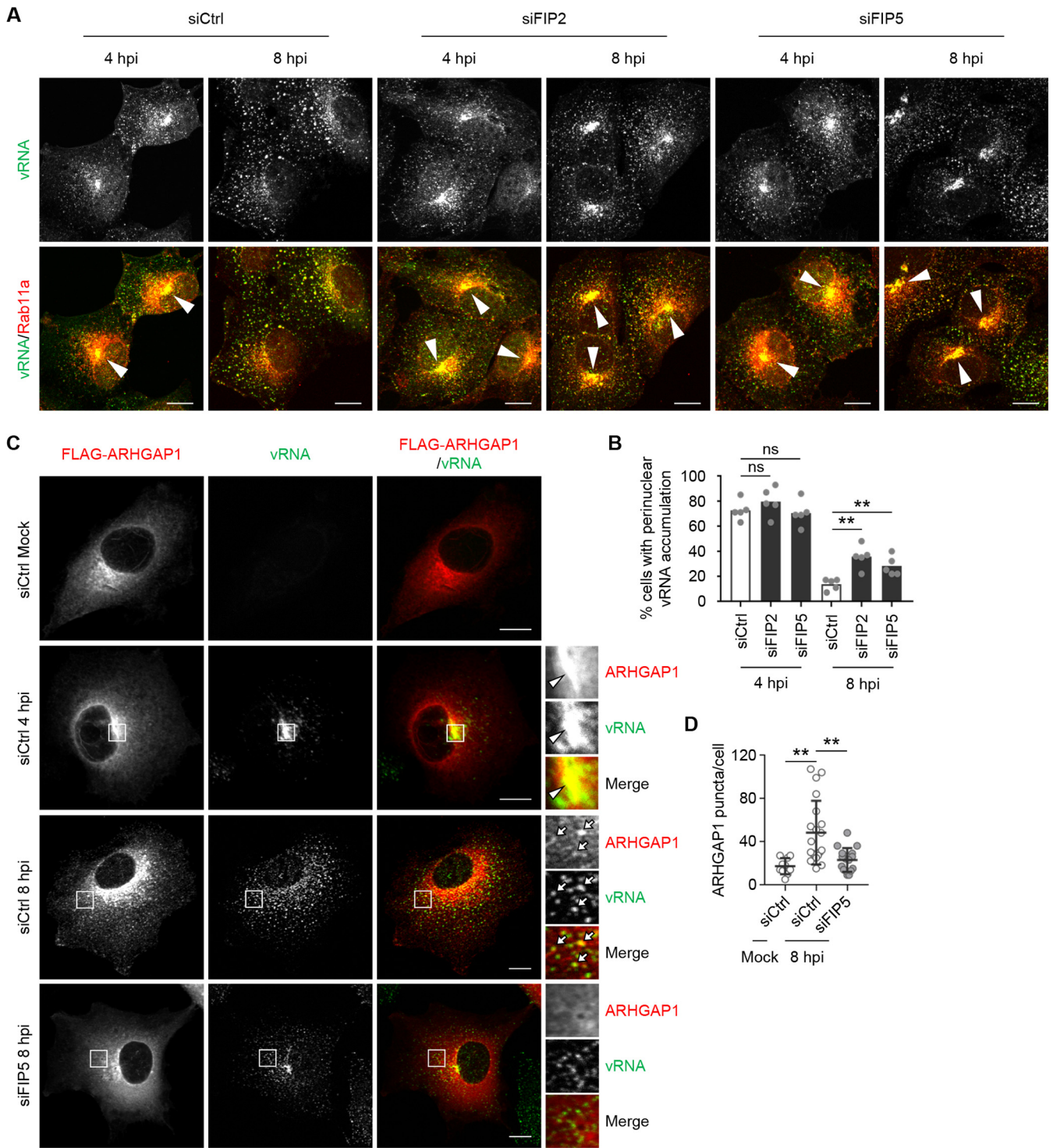


FIG 3 vRNPs reach to the plasma membrane together with ARHGAP1 in a FIP5-dependent manner. (A) A549 cells were transfected with scrambled (siCtrl), siFIP2 1, or siFIP5 1. At 48 h posttransfection, the cells were infected with PR8 virus at an MOI of 10. At 4 and 8 h postinfection, Rab11a (red) and seg7 vRNA (green) were visualized by indirect immunofluorescence assays and FISH assays. The arrowheads indicate ERCs. Representative images from three independent experiments are shown. (B) Percentage of cells showing the perinuclear accumulation of vRNA signal in panel A was measured ($n = 5$ fields with 60 to 113 cells/group). **, $P < 0.01$; one-way ANOVA with Tukey's test; ns, not significant. (C) FLAG-ARHGAP1-expressing A549 cells were transfected with scrambled (siCtrl) or siFIP5 1. At 48 h posttransfection, the cells were infected with PR8 virus at an MOI of 10. At 4 and 8 h postinfection, seg7 vRNA (green) and FLAG-ARHGAP1 (red) were visualized by FISH assays and indirect immunofluorescence assays with anti-FLAG antibody. Representative images from three independent experiments are shown. The arrowheads and arrows indicate ERCs and cytoplasmic punctate signals positive for FLAG-ARHGAP1 and vRNA, respectively. (D) The number of cytoplasmic FLAG-ARHGAP1 puncta in control or FIP5 KD cells of panel C were calculated using Imaris software (siCtrl mock, $n = 10$ cells; siCtrl at 8 hpi, $n = 20$ cells; siFIP5 at 8 hpi, $n = 16$ cells). Results are means \pm SDs. **, $P < 0.01$; one-way ANOVA with Tukey's test. Scale bars, 10 μ m (A and C).

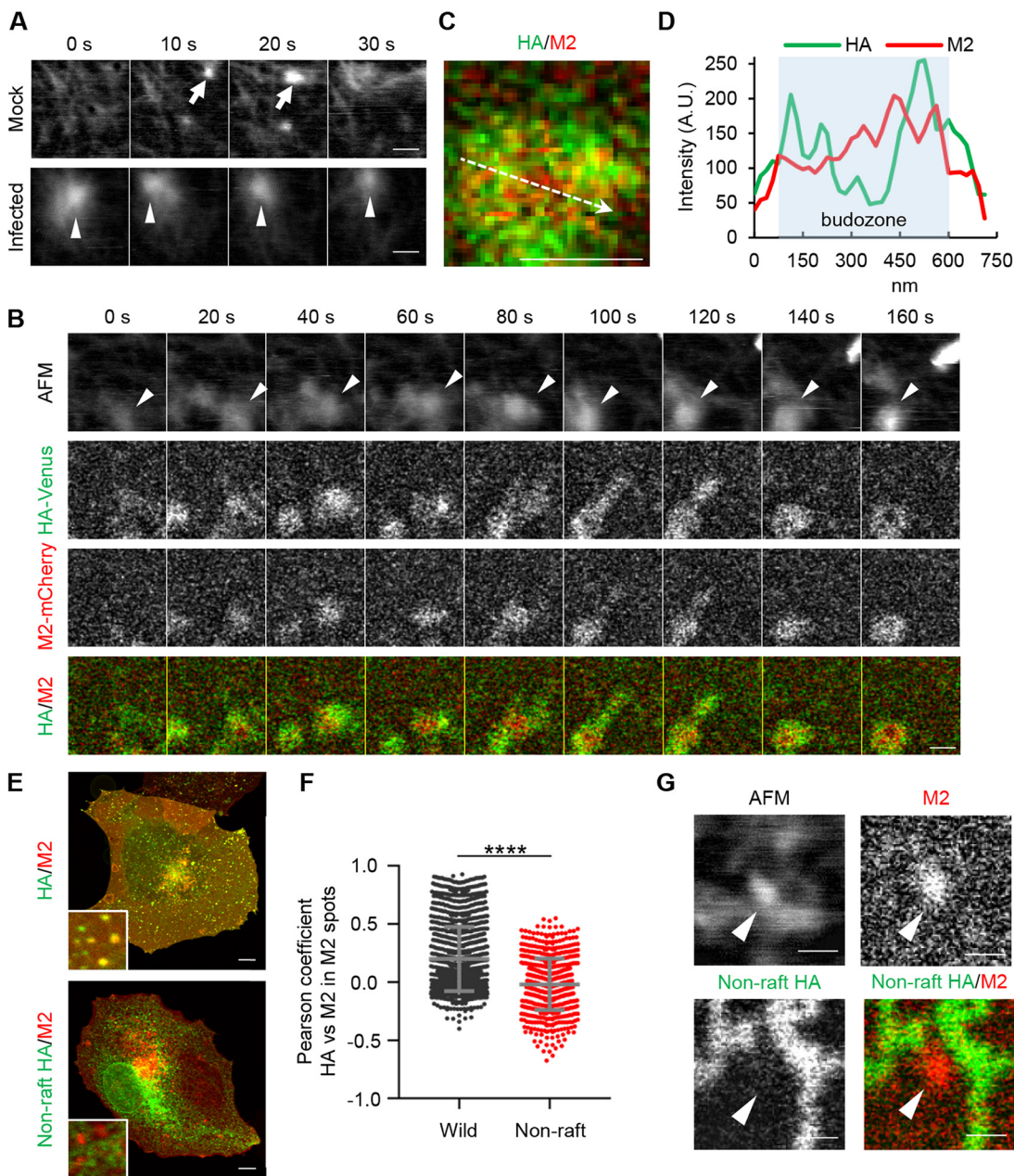


FIG 4 HS-AFM/fluorescence imaging of budzone-like protrusions. (A) COS-7 cells were infected with PR8 virus at an MOI of 10. At 12 h postinfection, the cells were subjected to time-lapse AFM imaging. (B) At 1 h posttransfection of plasmids expressing HA-Venus (green) and M2-mCherry (red), COS-7 cells were infected with PR8 virus. At 12 h postinfection, HS-AFM/fluorescence imaging studies were performed. (C) Enlarged image at 150 s after the observation in panel B. (D) Relative pixel intensities of M2-mCherry (red) and HA-Venus (green), along with the arrow, are shown. (E) Infected COS-7 cells expressing M2-mCherry (red) and nonraft HA-Venus (green) were observed by confocal microscopy. (F) The Pearson coefficient between the HA signal and M2 signal in each M2 spot is expressed. (G) Infected COS-7 cells expressing M2-mCherry (red) and either wild-type or nonraft HA-Venus (green) were observed by HS-AFM/fluorescence microscopy. Results are means \pm SDs. ****, $P < 0.0001$; two-tailed Student's t test. The arrows and arrowheads in panels A, B, and G indicate membrane ruffles and budzone-like protrusions, respectively. Scale bars, 500 nm (A, B, C, and G) or 10 μ m (E).

decreased to 68% of that of the control cells by FIP5 KD and to 56% by ARHGAP1 KD without impairing the apical transport of HA (Fig. 6A to C and Fig. S5A and B). These results indicated that the FIP5-mediated transport of ARHGAP1, together with vRNP, promotes the budzone formation at the plasma membrane. Note that newly synthesized HA and NA proteins are transported to the apical plasma membrane through the *trans*-Golgi network (TGN) in a Rab11a-independent manner (39, 42–44). It is also

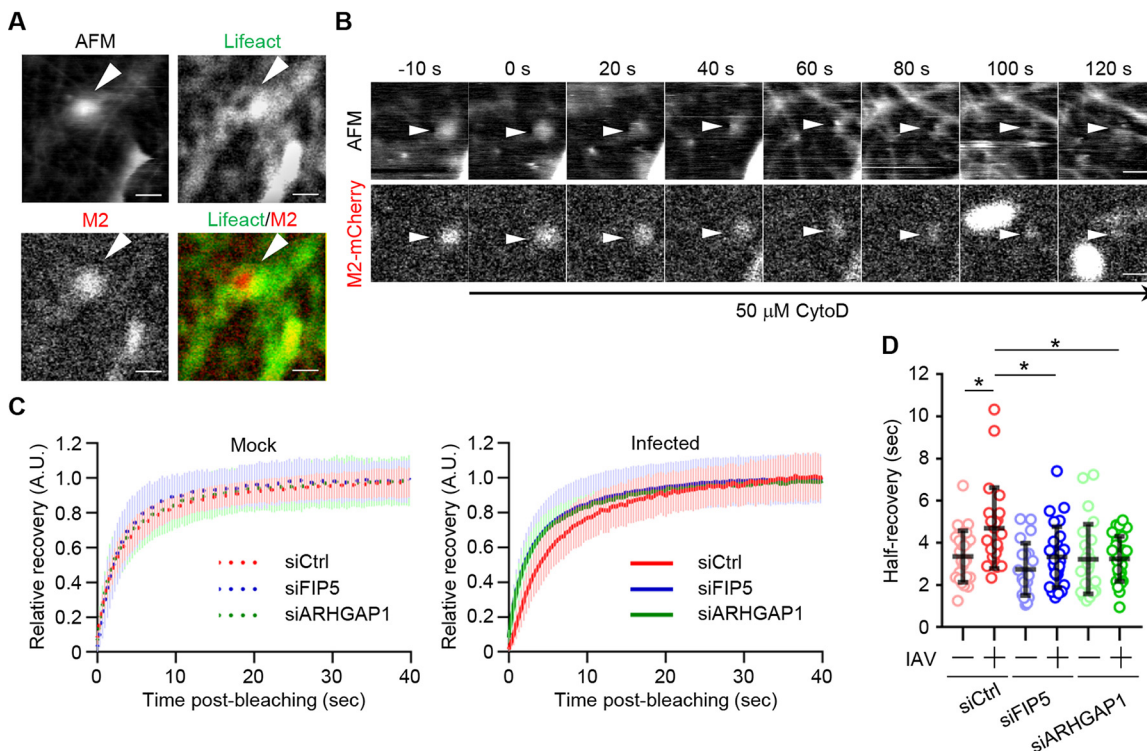


FIG 5 Viral budozone formation requires actin filaments stabilized by FIP5 and ARHGAP1. (A and B) COS-7 cells expressing Lifact-TagGFP2 (green) and M2-mCherry (red) (A) or M2-mCherry alone (B) were infected with PR8 virus. At 12 h postinfection, HS-AFM/fluorescence imaging studies were performed in the absence (A) or presence (B) of 50 μ M cytochalasin D (CytoD). The arrowheads indicate budozone-like protrusions. Scale bars, 500 nm. (C and D) At 12 h postinfection, the mobility of Lifact-TagGFP2 in A549 cells transfected with scrambled (siCtrl), siFIP5 1, or siARHGAP1 1 was analyzed by FRAP assays. (C) Relative fluorescence intensities of the bleached regions against the nonbleached regions are shown. (D) The mean half-recovery time was calculated using GraphPad Prism software ($n = 21$ to 28 cells/group). Results are means \pm SDs. *, $P < 0.05$; one-way ANOVA with Tukey's test.

reported that newly synthesized M2 protein is apically transported mainly by the Golgi apparatus (45) and in part by Rab11a-dependent endocytic transport (15). However, we found that FIP5 KD and ARHGAP1 KD had little effect on the surface M2 protein level (Fig. S5C and D). In line with the inhibition of budozone formation, the viral titers were reduced to 41% of the control cells by FIP5 KD and to 16% by ARHGAP1 KD (Fig. 7A). To quantitatively analyze the amount of HA on virions, virions were purified from the culture supernatants of infected cells treated with siFIP5 or siARHGAP1 by the ultracentrifugation through a sucrose cushion (Fig. 7B and C). The protein ratios of HA relative to M1, which is a scaffold protein of viral particles (16, 46–48), in purified virions obtained from FIP5 KD or ARHGAP1 KD cells were reduced to around 40% to 60% of those from control cells, respectively (Fig. 7B and C). Note that the HA/M1 ratio of virions obtained from FIP1 KD cells was unchanged (Fig. 7B and C). Note that TEM observations indicated that the purified virions from FIP5 KD cells and ARHGAP1 KD cells did not differ in the diameter of viral particles but contained fewer viral spike proteins than those from the control cells (Fig. S6A to C).

The intact viral particles are relatively resistant to digestion by proteases, and their epitopes are concentrated on the exposed surfaces, including the globular head domain, possibly due to steric hindrance of clustered HA. Thus, we assumed that the efficient HA packing on viral particles is important for the stability and the antigenic potential of viral particles. To address this possibility, the progeny viruses produced from control cells (vCtrl), FIP5 KD cells (vFIP5 KD), or ARHGAP1 KD cells (vARHGAP1 KD) were treated with chymotrypsin at a final concentration of 0, 0.1, or 1 μ g/mL. After incubation at 37°C for 3 h, the viral titer was determined by plaque assays. Although the progeny viruses from the control cells were resistant to the protease treatment,

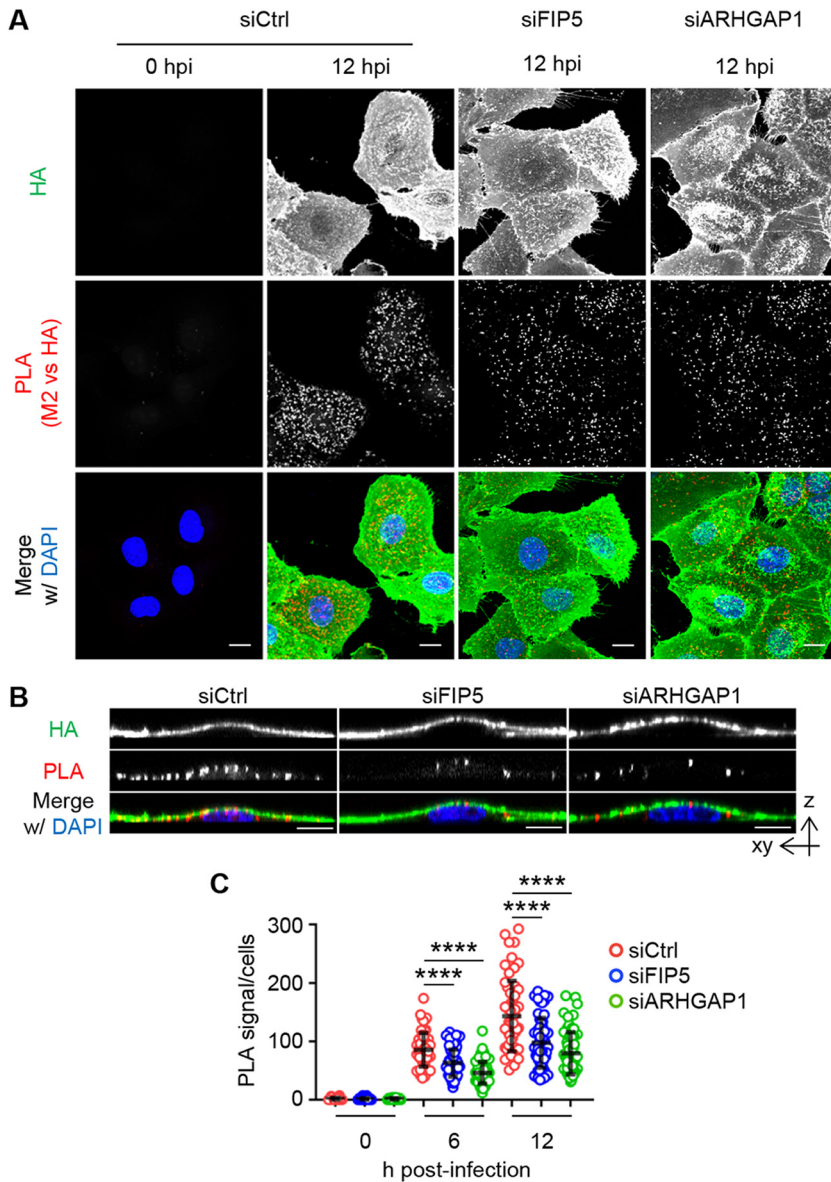


FIG 6 FIP5 and ARHGAP1 promote viral budzone formation. (A) A549 cells transfected with scrambled (siCtrl), siFIP5 1, or siARHGAP1 1 were infected with PR8 virus at an MOI of 10. At 6 and 12 h postinfection, the cells were subjected to PLA assays with anti-HA and anti-M2 antibodies (PLA signals, red). HA (green) and DNA (blue) were counterstained with anti-mouse IgG conjugated with Alexa 488 and DAPI (4',6-diamidino-2-phenylindole). (B) The vertical section images from the z-stack series of panel A were reconstructed. Representative images from three independent experiments are shown. (C) The number of PLA signals per cell in panel A were analyzed by Imaris software (means \pm SDs; $n = 50$ to 63 cells/group). ****, $P < 0.0001$; one-way ANOVA with Tukey's test.

the infectivity of progeny viruses from FIP5 KD or ARHGAP1 KD cells was reduced to around 40% of that of the control cells by addition of 1 μ g/mL chymotrypsin (Fig. 7D). We next examined the antigenic potential of progeny viral particles produced from control cells and FIP5 KD cells (Fig. 7E). Mice were intranasally immunized with formalin-inactivated virions containing 1 μ g of HA produced from control or FIP5 KD cells, and then the ratio of IAV-specific IgA against total IgA in nasal washes was quantified by enzyme-linked immunosorbent assay (ELISA). Because the viral titer was largely reduced in ARHGAP1 KD cells, we could not obtain a sufficient number of viral particles for the immunization (Fig. 7A). The level of anti-IAV IgA was elevated by approximately 1.48-fold through immunization with viral particles produced from FIP5 KD cells compared with that of the control (Fig. 7E). In addition, the IgA antibody obtained from

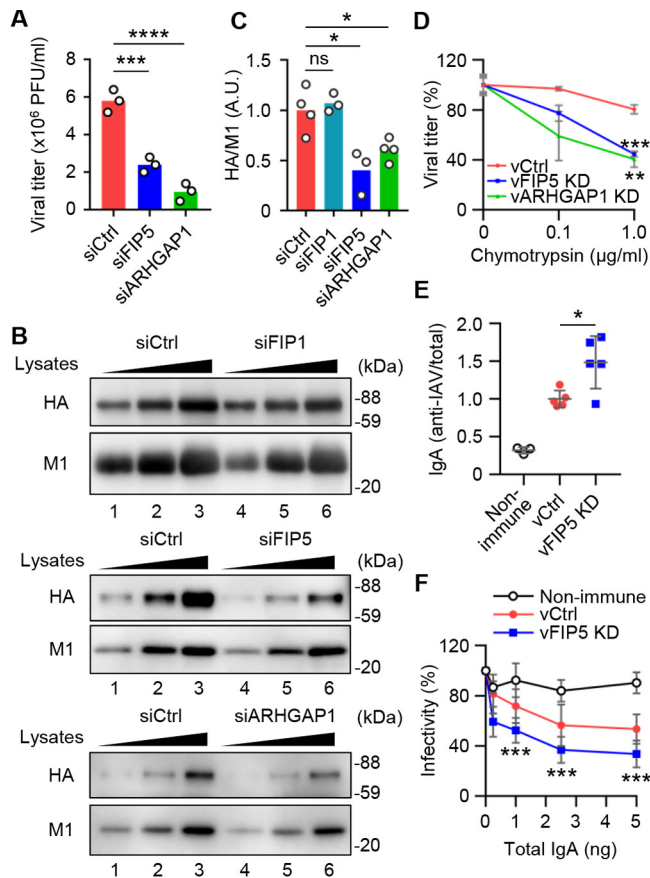


FIG 7 FIP5 and ARHGAP1 promote the production of stable progeny viral particles with reduced antigenicity. (A) A549 cells transfected with scrambled (siCtrl), siFIP5 1, or siARHGAP1 1 were infected with WSN virus at an MOI of 0.1. At 48 h postinfection, the viral titers in the culture supernatants were examined by plaque assays ($n = 3$, independent experiments). (B and C) Control, FIP1KD, FIP5 KD, and ARHGAP1 KD A549 cells were infected with WSN virus at an MOI of 0.1. At 48 h postinfection, the culture supernatants were ultracentrifuged through a 20% (wt/vol) sucrose cushion at $78,400 \times g$ for 1.5 h at 4°C . (B) The different volumes (2.5, 5, and $10 \mu\text{L}$) of purified viral particles were analyzed by SDS-PAGE followed by Western blot analyses with anti-HA and anti-M1 antibodies. (C) The relative amount of HA against M1 is shown ($n = 3$ or 4; independent experiments). (D) Virions produced from the control (vCtrl), FIP5 KD (vFIP5 KD), and ARHGAP1 KD (vARHGAP1) A549 cells were treated with chymotrypsin at a final concentration of 0, 0.1, or $1 \mu\text{g}/\text{mL}$ at 37°C for 3 h and then subjected to plaque assays. (E) The levels of IgA antibodies in nasal washes obtained from mice immunized with vCtrl or vFIP5 KD were determined by ELISA. The ratios of IAV-specific IgA against total IgA are shown ($n = 3$ to 5 mice per group). (F) PR8 virus was incubated with different concentrations of total IgA in nasal washes obtained from mice immunized with vCtrl or vFIP5 KD for 2 h. Each viral titer was determined by focus-forming assays with MDCK cells. The percentage of infected cells compared with the sample without nasal washes was represented as percentage of infectivity. *, $P < 0.05$; **, $P < 0.01$; ***, $P < 0.001$; ****, $P < 0.0001$; one-way ANOVA with Tukey's test (A, C, D, and F) or two-tailed Student's t test (E). Results are means \pm SDs (D to F).

mice immunized with FIP5 KD virions neutralized the virus infectivity by 1.4- to 2.2-fold higher than that of the control virions (Fig. 7F). These findings indicate that the efficient budding zone formation not only promotes the virus production but also increases the stability of viral particles and their protection against antibody responses.

DISCUSSION

Although Rab11 REs are required for the apical transport of progeny vRNPs, Rab11 effectors regulating the vRNP transport remained controversial. Our proteomics analysis revealed that Rab11a interacts with class I FIPs (FIP1C, FIP2, and FIP5) in infected cells (Fig. 1D). We found that both FIP2 and FIP5 proteins are colocalized with vRNPs in ERCS and are required for the transport of vRNPs to the plasma membrane through the endocytic vesicles emanated from the ERCS (Fig. 2 and 3). It is reported that FIP2 forms a homodimer through the N-terminal C2 domain, which is highly conserved in class I FIPs (26, 49). Further,

class I FIPs form heterodimers in the yeast two-hybrid system (50). On the basis of these results, FIP2 and FIP5 likely form a heterodimer and then regulate the kinesin-dependent anterograde transport of vRNPs. However, it is reported that transiently expressed full-length or truncated FIPs inhibited the ectopic localization of NP to the mitochondria expressing Rab11a fused to the mitochondria-targeting signal (29), suggesting that FIPs may compete with vRNPs for Rab11a binding. It is also proposed that KIF13, a kinesin family motor, binds to Rab11a and may directly regulate the intracellular transport of vRNPs (51). Further analysis is needed to understand the FIP-dependent and -independent pathways for the spatiotemporal regulation of vRNP transport.

In this study, the high-speed atomic force/fluorescence microscopy system enabled time-lapse imaging of budzone formation. The viral budzone was assembled in a lipid raft-dependent manner through the stabilization of actin filaments beneath the plasma membrane (Fig. 4 and 5). In COS-7 cells, we found that the viral budzone was surrounded by cortical actin filaments (Fig. 5A). Although the mesh size and filament orientation of cortical actin differ among the cell types used (52), such actin filaments, called actin vortices, are known to be highly stable but plastic higher-order structures (53). The cortical actin mesh is required for the formation of lipid rafts through the triggering of the liquid-ordered and liquid-disordered phase separation (54). Further, the lateral clustering of membrane proteins localized in the lipid raft is dependent on the contraction of cortical actin (40, 41). It has been reported that the mobility of HA decreases in regions with high densities of actin filaments and that the treatment with latrunculin A, a cortical actin-disrupting agent, dispersed the HA clusters on the plasma membrane (55). The reorganization of actin filaments is mainly regulated by Arp2/3, an actin-nucleating protein regulated by Cdc42, and MyoII, a molecular motor protein that reversibly cross-links actin filaments regulated by RhoA (56). Our findings revealed that the dynamics of cortical actin were stabilized by ARHGAP1, a negative regulator of Rho family proteins, upon IAV infection (Fig. 5C and D). Thus, it is possible that Rab11a REs mediate the apical transport of vRNPs with signal regulators, including cholesterol (35) and ARHGAP1, to trigger the budzone formation concomitantly with vRNP transport to the plasma membrane.

Although morphologic abnormalities were observed in virions produced from Rab11a KD cells, the biological significance has not been understood (57). In this study, we showed that the efficient budzone formation is crucial for the protease resistance and reduced antigenic potential of viral particles, possibly through the steric hindrance effect of clustered HA (Fig. 7D). HA consists of a globular head domain and a stalk domain. Most neutralizing antibodies recognize highly antigenic variable regions in the globular head domain, but not in other regions, including the stalk domain (58–60), possibly due to the fact that the other regions are hidden by clustering viral membrane proteins on the viral particles (61). Our findings contribute to the understanding of viral immune evasion strategy through the structural integrity of the viral particles, possibly by the efficient budzone formation.

MATERIALS AND METHODS

Affinity capture of biotinylated proteins. At 2 h postinfection, myc-BirA*-Rab11a-expressing A549 cells were cultured with 50 μ M biotin for 6 h. At 8 h postinfection, the cells were lysed in lysis buffer 1 (50 mM Tris-HCl, pH 7.4, 150 mM NaCl, 1% NP-40, 0.5% sodium deoxycholate, 2 mM MgCl₂, 20 U Benzonase [Merck; catalog no. 70746], and complete protease inhibitor [Roche]) at 4°C for 5 min and then further lysed with lysis buffer 2 (50 mM Tris-HCl, pH 7.4, 150 mM NaCl, 1% NP-40, 0.5% sodium deoxycholate, 2 mM Tris(2-carboxyethyl)phosphine hydrochloride [TCEP], 0.2% SDS, and 2 mM EDTA). The soluble fractions were subjected to pulldown assays using streptavidin magnetic beads (TriLink; catalog no. M-1002). After being washed with wash buffers 1 to 4 (wash buffer 1, 50 mM Tris-HCl, pH 7.4, and 2% SDS; wash buffer 2, 20 mM Tris-HCl, pH 7.4, 500 mM NaCl, 1% Triton X-100, 0.1% sodium deoxycholate, and 1 mM EDTA; wash buffer 3, 10 mM Tris-HCl, pH 7.4, 250 mM LiCl, 1% NP-40, 0.1% sodium deoxycholate, and 1 mM EDTA; and wash buffer 4, 50 mM Tris-HCl, pH 7.4), the beads were incubated in an elution buffer (5 mM biotin, 150 mM NaCl, 2% SDS, and 5 mM TCEP) at 100°C for 5 min. The eluted proteins were subjected to LC-MS analysis using a Q Exactive HF-X mass spectrometer (Thermo Fisher Scientific). Gene ontology analysis of the identified proteins was performed using the DAVID database version 6.8.

Intracellular localization of the viral genome and viral/cellular proteins. Fluorescence *in situ* hybridization (FISH) assays and indirect immunofluorescence assays were carried out as previously described (62). The cells were fixed with 4% paraformaldehyde (PFA) for 10 min and permeabilized with 0.5% Triton X-100 in phosphate-buffered saline (PBS) for 5 min. After being incubated in PBS containing 1% bovine serum albumin for 30 min, the coverslips were incubated with each antibody for 1 h and

then further incubated with Alexa Fluor 405-, 488-, and 568-conjugated secondary antibodies, respectively (Thermo Fisher Scientific). The permeabilization procedure was omitted for the staining of cell surface M2. FISH assays were performed after indirect immunofluorescence assays using an RNA probe complementary to the segment 7 virus genome. Images were acquired by confocal laser scanning microscopy (Carl Zeiss; LSM700) using an $\times 63$ Apochromat objective (numerical aperture [NA], 1.4). The percentage of cytoplasmic vRNA signals colocalized with FIPs, excluding those localized around the ERC, the number of punctate ARHGAP1 signals in the cytoplasm, and the intensity of M2 signals on the cell surface, was calculated using Imaris software (Bitplane). Pearson's correlation coefficient of HA and M2 signals was calculated using the Fiji distribution of ImageJ software (63) with the Coloc 2 plugin.

Gene silencing mediated by siRNA. Short interfering RNAs (siRNAs) against *RAB11FIP1* (siRNA ID HSS149439), *RAB11FIP2* (1, siRNA ID HSS117714, and 2, siRNA ID HSS117713), *RAB11FIP5* (1, siRNA ID HSS178037, and 2, siRNA ID HSS119747), and *ARHGAP1* (1, siRNA ID HSS100669, and 2, siRNA ID HSS100671) genes were purchased (Thermo Fisher Scientific), and their transfection was carried out using Lipofectamine RNAi Max (Thermo Fisher Scientific) according to the manufacturer's protocol.

Proximity ligation assays. The quantification of budding formation by proximity ligation assays (PLAs) was carried out as previously described (64). Briefly, cells were fixed with 4% PFA and then blocked with 1% milk for 30 min. The cells were incubated with mouse anti-HA antibody for 1 h and fixed again with 4% PFA. After permeabilization with 0.5% Triton X-100 for 5 min, the cells were further incubated with rabbit anti-M2 antibody for 1 h. PLA was carried out using a Duolink *in situ* PLA kit (Sigma) according to the manufacturer's protocol. The number of PLA signals was measured using Imaris software.

Transmission electron microscopy. Preprocessing of the virions for TEM was carried out referring to a previously reported protocol (65). At 48 h postinfection of the WSN strain, the culture supernatants of A549 cells were centrifuged at $900 \times g$ for 5 min at 4°C and then fixed with 2.5% glutaraldehyde at 4°C for 1 h followed by filtration using a 0.22- μm filter. The fixed viral particles were ultracentrifuged through a 20% (wt/vol) sucrose cushion at $78,400 \times g$ for 1.5 h at 4°C. The purified virions were absorbed into hydrophilized acrylic-coated copper mesh grids (Okenshoji; catalog no. MMA-C10) and negatively stained with 2% phosphotungstic acid solution pH 5.8. Images were acquired using a JEM-1400 (Jeol). The diameter of viral particles and the number of spherical viral spike proteins with a diameter larger than 2.5 nm on the viral particles were measured manually using Fiji/ImageJ software (63).

High-speed atomic force/fluorescence microscopic imaging. A tip-scan high-speed atomic force microscope (AFM) equipped with an inverted confocal microscope (Olympus; BIXAM) was used as previously described (52, 66, 67). We used COS-7 cells as appropriate cells for the BIXAM imaging because they show high transfection efficiency and have a relatively flatter cell surface than epithelial cells. At 1 h posttransfection of HA-Venus and M2-mCherry, COS-7 cells were infected with the PR8 strain at an MOI of 10. At 12 h postinfection, images were acquired using BIXAM at 28°C with the phase modulation mode using an electron beam-deposited sharp cantilever tip with a spring constant of 0.05 nm^{-1} (USC-F0.8-k0.05; a customized cantilever purchased from NanoWorld). The confocal images and AFM images were simultaneously acquired at a scanning rate of 10 s/frame.

Fluorescence recovery after photobleaching analysis. A549 cells stably expressing Lifeact-TagGFP2 were infected with PR8 strain at an MOI of 10. At 12 h postinfection, FRAP analysis was performed with a 488-nm laser. The bleaching routine started with 2 prebleach scans followed by a bleaching scan. Then, the recovery of fluorescence was monitored every 300 ms for 40 s at 0.2% laser intensity. The fluorescence recovery data were normalized using data acquired from the nonbleached regions. To calculate the half-recovery time, the FRAP curves were fitted with the one-phase exponential equation using GraphPad Prism (version 7.03).

Mouse models. All the *in vivo* experiments were carried out according to the Guideline for Proper Conduct of Animal Experiments of the Science Council of Japan. The protocols for the animal experiments were approved by the Animal Care and Use Committee of the University of Tsukuba. Eight- to 10-week-old wild-type female C57BL/6J Jcl mice purchased from Clea Japan were used.

Immunization of inactivated virions. The viral particles (PR8) produced from FIP5 KD cells were concentrated by ultracentrifugation as described above. The purified virions were fixed with 0.1% formalin/PBS at 4°C for a week. Mice were intranasally immunized with inactivated virions equivalent to 1 μg of HA in the presence of 10 μg of poly(I:C) (InvivoGen; catalog code tlr-pic) under anesthesia by intraperitoneal injection of pentobarbital sodium (Kyoritsu Seiyaku). The mice were reimmunized twice weekly, and the nasal washes were collected 1 week after the final immunization. The levels of total IgA and anti-IAV IgA antibodies were determined by ELISA as described previously (68).

Neutralization assay. Nasal wash samples containing equal amounts of total IgA in each sample were incubated with 4×10^4 PFU of the PR8 strain at 37°C for 2 h. Then, the mixtures were inoculated into MDCK cells. At 4 h postinfection, the cells were fixed in 4% PFA, and the viral titers were determined by focus-forming assays with anti-NP antibody as described previously (69). The viral titer of viruses treated with nasal wash was represented as percentage of infectivity relative to that of untreated viruses.

Statistical analysis. The statistical significance of experimental results was determined by an unpaired two-tailed Student's *t* test or a one-way analysis of variance (ANOVA) with Tukey's test using GraphPad Prism (version 7.03). ns, not significant; *, $P < 0.05$; **, $P < 0.01$; ***, $P < 0.001$; ****, $P < 0.0001$.

SUPPLEMENTAL MATERIAL

Supplemental material is available online only.

TEXT S1, DOCX file, 0.04 MB.

FIG S1, TIF file, 0.1 MB.

FIG S2, TIF file, 0.8 MB.

FIG S3, TIF file, 1.1 MB.

FIG S4, TIF file, 0.3 MB.

FIG S5, TIF file, 0.9 MB.

FIG S6, TIF file, 0.4 MB.

TABLE S1, XLSX file, 0.1 MB.

ACKNOWLEDGMENTS

We thank F. Miyamasu (Medical English Communications Center, University of Tsukuba) for critical review of the manuscript.

This work was supported in part by grants-in-aid from the Ministry of Education, Culture, Sports, Science and Technology of Japan (19J20101 to T.K. and 16H05192 and 19H03475 to A.K.); the Research Program on Emerging and Re-emerging Infectious Diseases (JP20fk0108076h0003 to A.K.); the Japan Program for Infectious Diseases Research and Infrastructure (JP20wm0325019h0001 to A.K.); the Japan Agency for Medical Research and Development, CREST and COI-NEXT from the Japan Science and Technology Agency (JPMJCR20H6 and JPMJPF2017 to A.K.); the Takeda Science Foundation (to A.K.); and the NOMURA Microbial Community Control Project of ERATO, Japanese Science and Technology Agency (to A.K.).

T.H., K.N., and A.K. conceived and designed the experiments. T.K., T.H., T.N., N.S., A.Y., K.K., and A.K. performed the experiments and analyzed the data. T.K. and A.K. wrote the manuscript. We declare no conflicts of interest.

REFERENCES

- Moules V, Terrier O, Yver M, Riteau B, Moriscot C, Ferraris O, Julien T, Giudice E, Rolland JP, Erny A, Bouscambert-Duchamp M, Frobert E, Roscalatrava M, Pu Lin Y, Hay A, Thomas D, Schoehn G, Lina B. 2011. Importance of viral genomic composition in modulating glycoprotein content on the surface of influenza virus particles. *Virology* 414:51–62. <https://doi.org/10.1016/j.virol.2011.03.011>.
- Wasilewski S, Calder LJ, Grant T, Rosenthal PB. 2012. Distribution of surface glycoproteins on influenza A virus determined by electron cryotomography. *Vaccine* 30:7368–7373. <https://doi.org/10.1016/j.vaccine.2012.09.082>.
- Schmitt AP, Lamb RA. 2005. Influenza virus assembly and budding at the viral budzone. *Adv Virus Res* 64:383–416. [https://doi.org/10.1016/S0065-3527\(05\)64012-2](https://doi.org/10.1016/S0065-3527(05)64012-2).
- Amorim MJ, Bruce EA, Read EK, Foeglein A, Mahen R, Stuart AD, Digard P. 2011. A Rab11- and microtubule-dependent mechanism for cytoplasmic transport of influenza A virus viral RNA. *J Virol* 85:4143–4156. <https://doi.org/10.1128/JVI.02606-10>.
- Momose F, Sekimoto T, Ohkura T, Jo S, Kawaguchi A, Nagata K, Morikawa Y. 2011. Apical transport of influenza A virus ribonucleoprotein requires Rab11-positive recycling endosome. *PLoS One* 6:e21123. <https://doi.org/10.1371/journal.pone.0021123>.
- Kawaguchi A, Matsumoto K, Nagata K. 2012. YB-1 functions as a porter to lead influenza virus ribonucleoprotein complexes to microtubules. *J Virol* 86:11086–11095. <https://doi.org/10.1128/JVI.00453-12>.
- Nturibi E, Bhagwat AR, Coburn S, Myerburg MM, Lakdawala SS. 2017. Intracellular colocalization of influenza viral RNA and Rab11A is dependent upon microtubule filaments. *J Virol* 91:e01179-17. <https://doi.org/10.1128/JVI.01179-17>.
- Suomalainen M. 2002. Lipid rafts and assembly of enveloped viruses. *Traffic* 3:705–709. <https://doi.org/10.1034/j.1600-0854.2002.31002.x>.
- Pike LJ. 2006. Rafts defined: a report on the Keystone symposium on lipid rafts and cell function. *J Lipid Res* 47:1597–1598. <https://doi.org/10.1194/jlr.E600002-JLR200>.
- Zhang J, Pekosz A, Lamb RA. 2000. Influenza virus assembly and lipid raft microdomains: a role for the cytoplasmic tails of the spike glycoproteins. *J Virol* 74:4634–4644. <https://doi.org/10.1128/jvi.74.10.4634-4644.2000>.
- Leser GP, Lamb RA. 2005. Influenza virus assembly and budding in raft-derived microdomains: a quantitative analysis of the surface distribution of HA, NA and M2 proteins. *Virology* 342:215–227. <https://doi.org/10.1016/j.virol.2005.09.049>.
- Hess ST, Kumar M, Verma A, Farrington J, Kenworthy A, Zimmerberg J. 2005. Quantitative electron microscopy and fluorescence spectroscopy of the membrane distribution of influenza hemagglutinin. *J Cell Biol* 169:965–976. <https://doi.org/10.1083/jcb.200412058>.
- Veit M, Klenk HD, Kendal A, Rott R. 1991. The M2 protein of influenza A virus is acylated. *J Gen Virol* 72:1461–1465. <https://doi.org/10.1099/0022-1317-72-6-1461>.
- Schroeder C, Heider H, Moncke-Buchner E, Lin TL. 2005. The influenza virus ion channel and maturation cofactor M2 is a cholesterol-binding protein. *Eur Biophys J* 34:52–66. <https://doi.org/10.1007/s00249-004-0424-1>.
- Rossman JS, Jing X, Leser GP, Lamb RA. 2010. Influenza virus M2 protein mediates ESCRT-independent membrane scission. *Cell* 142:902–913. <https://doi.org/10.1016/j.cell.2010.08.029>.
- Ali A, Avalos RT, Ponimaskin E, Nayak DP. 2000. Influenza virus assembly: effect of influenza virus glycoproteins on the membrane association of M1 protein. *J Virol* 74:8709–8719. <https://doi.org/10.1128/JVI.74.18.8709-8719.2000>.
- Liu T, Muller J, Ye Z. 2002. Association of influenza virus matrix protein with ribonucleoproteins may control viral growth and morphology. *Virology* 304:89–96. <https://doi.org/10.1006/viro.2002.1669>.
- Stenmark H. 2009. Rab GTPases as coordinators of vesicle traffic. *Nat Rev Mol Cell Biol* 10:513–525. <https://doi.org/10.1038/nrm2728>.
- Mizuno-Yamasaki E, Rivera-Molina F, Novick P. 2012. GTPase networks in membrane traffic. *Annu Rev Biochem* 81:637–659. <https://doi.org/10.1146/annurev-biochem-052810-093700>.
- Bos JL, Rehmann H, Wittinghofer A. 2007. GEFs and GAPs: critical elements in the control of small G proteins. *Cell* 129:865–877. <https://doi.org/10.1016/j.cell.2007.05.018>.
- Barr F, Lambright DG. 2010. Rab GEFs and GAPs. *Curr Opin Cell Biol* 22:461–470. <https://doi.org/10.1016/j.cob.2010.04.007>.
- Grosshans BL, Ortiz D, Novick P. 2006. Rabs and their effectors: achieving specificity in membrane traffic. *Proc Natl Acad Sci U S A* 103:11821–11827. <https://doi.org/10.1073/pnas.0601617103>.
- Maxfield FR, McGraw TE. 2004. Endocytic recycling. *Nat Rev Mol Cell Biol* 5:121–132. <https://doi.org/10.1038/nrm1315>.
- Lin SX, Gundersen GG, Maxfield FR. 2002. Export from pericentriolar endocytic recycling compartment to cell surface depends on stable, detyrosinated (Glu) microtubules and kinesin. *Mol Biol Cell* 13:96–109. <https://doi.org/10.1091/mbc.01-05-0224>.
- Horgan CP, McCaffrey MW. 2009. The dynamic Rab11-FIPs. *Biochem Soc Trans* 37:1032–1036. <https://doi.org/10.1042/BST0371032>.
- Hales CM, Vaerman JP, Goldenring JR. 2002. Rab11 family interacting protein 2 associates with Myosin Vb and regulates plasma membrane recycling. *J Biol Chem* 277:50415–50421. <https://doi.org/10.1074/jbc.M209270200>.

27. Schonteich E, Wilson GM, Burden J, Hopkins CR, Anderson K, Goldenring JR, Prekeris R. 2008. The Rip11/Rab11-FIP5 and kinesin II complex regulates endocytic protein recycling. *J Cell Sci* 121:3824–3833. <https://doi.org/10.1242/jcs.032441>.
28. Horgan CP, Hanscom SR, Jolly RS, Futter CE, McCaffrey MW. 2010. Rab11-FIP3 links the Rab11 GTPase and cytoplasmic dynein to mediate transport to the endosomal-recycling compartment. *J Cell Sci* 123:181–191. <https://doi.org/10.1242/jcs.052670>.
29. Vale-Costa S, Alenquer M, Sousa AL, Kellen B, Ramalho J, Tranfield EM, Amorim MJ. 2016. Influenza A virus ribonucleoproteins modulate host recycling by competing with Rab11 effectors. *J Cell Sci* 129:1697–1710. <https://doi.org/10.1242/jcs.188409>.
30. Chapman-Smith A, Cronan JE, Jr. 1999. The enzymatic biotinylation of proteins: a post-translational modification of exceptional specificity. *Trends Biochem Sci* 24:359–363. [https://doi.org/10.1016/S0968-0004\(99\)01438-3](https://doi.org/10.1016/S0968-0004(99)01438-3).
31. Roux KJ, Kim DI, Raida M, Burke B. 2012. A promiscuous biotin ligase fusion protein identifies proximal and interacting proteins in mammalian cells. *J Cell Biol* 196:801–810. <https://doi.org/10.1083/jcb.201112098>.
32. Barford ET, Zheng Y, Kuang WJ, Hart MJ, Evans T, Cerione RA, Ashkenazi A. 1993. Cloning and expression of a human CDC42 GTPase-activating protein reveals a functional SH3-binding domain. *J Biol Chem* 268:26059–26062. [https://doi.org/10.1016/S0021-9258\(19\)74277-X](https://doi.org/10.1016/S0021-9258(19)74277-X).
33. Muller PM, Rademacher J, Bagshaw RD, Wortmann C, Barth C, van Unen J, Alp KM, Giudice G, Eccles RL, Heinrich LE, Pascual-Vargas P, Sanchez-Castro M, Brandenburg L, Mbamalu G, Tucholska M, Spatt L, Czajkowski MT, Welke RW, Zhang S, Nguyen V, Rrustemi T, Trnka P, Freitag K, Larsen B, Popp O, Mertins P, Gingras AC, Roth FP, Colwill K, Bakal C, Pertz O, Pawson T, Petsalaki E, Rocks O. 2020. Systems analysis of RhoGEF and RhoGAP regulatory proteins reveals spatially organized RAC1 signalling from integrin adhesions. *Nat Cell Biol* 22:498–511. <https://doi.org/10.1038/s41556-020-0488-x>.
34. Sirokmany G, Szidonya L, Kaldi K, Gaborik Z, Ligeti E, Geiszt M. 2006. Sec14 homology domain targets p50RhoGAP to endosomes and provides a link between Rab and Rho GTPases. *J Biol Chem* 281:6096–6105. <https://doi.org/10.1074/jbc.M510619200>.
35. Kawaguchi A, Hirohama M, Harada Y, Osari S, Nagata K. 2015. Influenza virus induces cholesterol-enriched endocytic recycling compartments for budzone formation via cell cycle-independent centrosome maturation. *PLoS Pathog* 11:e1005284. <https://doi.org/10.1371/journal.ppat.1005284>.
36. Veit M, Thaa B. 2011. Association of influenza virus proteins with membrane rafts. *Adv Virol* 2011:370606. <https://doi.org/10.1155/2011/370606>.
37. Leser GP, Lamb RA. 2017. Lateral organization of influenza virus proteins in the budzone region of the plasma membrane. *J Virol* 91:e02104-16. <https://doi.org/10.1128/JVI.02104-16>.
38. Takeda M, Leser GP, Russell CJ, Lamb RA. 2003. Influenza virus hemagglutinin concentrates in lipid raft microdomains for efficient viral fusion. *Proc Natl Acad Sci U S A* 100:14610–14617. <https://doi.org/10.1073/pnas.2235620100>.
39. Ohkura T, Momose F, Ichikawa R, Takeuchi K, Morikawa Y. 2014. Influenza A virus hemagglutinin and neuraminidase mutually accelerate their apical targeting through clustering of lipid rafts. *J Virol* 88:10039–10055. <https://doi.org/10.1128/JVI.00586-14>.
40. Oliferenko S, Pailha K, Harder T, Gerke V, Schwarzler C, Schwarz H, Beug H, Gunthert U, Huber LA. 1999. Analysis of CD44-containing lipid rafts: recruitment of annexin II and stabilization by the actin cytoskeleton. *J Cell Biol* 146:843–854. <https://doi.org/10.1083/jcb.146.4.843>.
41. Gowrishankar K, Ghosh S, Saha S, C R, Mayor S, Rao M. 2012. Active remodeling of cortical actin regulates spatiotemporal organization of cell surface molecules. *Cell* 149:1353–1367. <https://doi.org/10.1016/j.cell.2012.05.008>.
42. Roberts PC, Garten W, Klenk HD. 1993. Role of conserved glycosylation sites in maturation and transport of influenza A virus hemagglutinin. *J Virol* 67:3048–3060. <https://doi.org/10.1128/JVI.67.6.3048-3060.1993>.
43. Nayak DP, Hui EK, Barman S. 2004. Assembly and budding of influenza virus. *Virus Res* 106:147–165. <https://doi.org/10.1016/j.virusres.2004.08.012>.
44. York IA, Stevens J, Alymova IV. 2019. Influenza virus N-linked glycosylation and innate immunity. *Biosci Rep* 39:BSR20171505. <https://doi.org/10.1042/BSR20171505>.
45. Zhu P, Liang L, Shao X, Luo W, Jiang S, Zhao Q, Sun N, Zhao Y, Li J, Wang J, Zhou Y, Zhang J, Wang G, Jiang L, Chen H, Li C. 2017. Host cellular protein TRAPP6ADelta interacts with influenza A virus M2 protein and regulates viral propagation by modulating M2 trafficking. *J Virol* 91:e01757-16. <https://doi.org/10.1128/JVI.01757-16>.
46. Li S, Xu M, Coelingh K. 1995. Electroporation of influenza virus ribonucleoprotein complexes for rescue of the nucleoprotein and matrix genes. *Virus Res* 37:153–161. [https://doi.org/10.1016/0168-1702\(95\)00031-k](https://doi.org/10.1016/0168-1702(95)00031-k).
47. Liu C, Eichelberger MC, Compans RW, Air GM. 1995. Influenza type A virus neuraminidase does not play a role in viral entry, replication, assembly, or budding. *J Virol* 69:1099–1106. <https://doi.org/10.1128/JVI.69.2.1099-1106.1995>.
48. Pattnaik AK, Brown DJ, Nayak DP. 1986. Formation of influenza virus particles lacking hemagglutinin on the viral envelope. *J Virol* 60:994–1001. <https://doi.org/10.1128/JVI.60.3.994-1001.1986>.
49. Lindsay AJ, McCaffrey MW. 2004. The C2 domains of the class I Rab11 family of interacting proteins target recycling vesicles to the plasma membrane. *J Cell Sci* 117:4365–4375. <https://doi.org/10.1242/jcs.01280>.
50. Wallace DM, Lindsay AJ, Hendrick AG, McCaffrey MW. 2002. The novel Rab11-FIP/Rip/RCP family of proteins displays extensive homo- and hetero-interacting abilities. *Biochem Biophys Res Commun* 292:909–915. <https://doi.org/10.1006/bbrc.2002.6736>.
51. Ramos-Nascimento A, Kellen B, Ferreira F, Alenquer M, Vale-Costa S, Raposo G, Delevoe C, Amorim MJ. 2017. KIF13A mediates trafficking of influenza A virus ribonucleoproteins. *J Cell Sci* 130:4038–4050. <https://doi.org/10.1242/jcs.210807>.
52. Zhang Y, Yoshida A, Sakai N, Uekusa Y, Kumeta M, Yoshimura SH. 2017. In vivo dynamics of the cortical actin network revealed by fast-scanning atomic force microscopy. *Microscopy (Oxf)* 66:272–282. <https://doi.org/10.1093/jmicro/dfx015>.
53. Fritzsche M, Li D, Colin-York H, Chang VT, Moendarbary E, Felce JH, Sezgin E, Charras G, Betzig E, Eggeling C. 2017. Self-organizing actin patterns shape membrane architecture but not cell mechanics. *Nat Commun* 8:14347. <https://doi.org/10.1038/ncomms14347>.
54. Liu AP, Fletcher DA. 2006. Actin polymerization serves as a membrane domain switch in model lipid bilayers. *Biophys J* 91:4064–4070. <https://doi.org/10.1529/biophysj.106.090852>.
55. Gudheti MV, Curthoys NM, Gould TJ, Kim D, Gunewardene MS, Gabor KA, Gosse JA, Kim CH, Zimmerberg J, Hess ST. 2013. Actin mediates the nanoscale membrane organization of the clustered membrane protein influenza hemagglutinin. *Biophys J* 104:2182–2192. <https://doi.org/10.1016/j.bpj.2013.03.054>.
56. Colin-York H, Li D, Korobchevskaya K, Chang VT, Betzig E, Eggeling C, Fritzsche M. 2019. Cytoskeletal actin patterns shape mast cell activation. *Commun Biol* 2:93. <https://doi.org/10.1038/s42003-019-0322-9>.
57. Bruce EA, Digard P, Stuart AD. 2010. The Rab11 pathway is required for influenza A virus budding and filament formation. *J Virol* 84:5848–5859. <https://doi.org/10.1128/JVI.00307-10>.
58. Thyagarajan B, Bloom JD. 2014. The inherent mutational tolerance and antigenic evolvability of influenza hemagglutinin. *Elife* 3:e03300. <https://doi.org/10.7554/eLife.03300>.
59. Heaton NS, Sachs D, Chen CJ, Hai R, Palese P. 2013. Genome-wide mutagenesis of influenza virus reveals unique plasticity of the hemagglutinin and NS1 proteins. *Proc Natl Acad Sci U S A* 110:20248–20253. <https://doi.org/10.1073/pnas.1320524110>.
60. Treanor JJ. 2016. Clinical practice. Influenza vaccination. *N Engl J Med* 375:1261–1268. <https://doi.org/10.1056/NEJMcip1512870>.
61. Kirkpatrick E, Qiu X, Wilson PC, Bahl J, Krammer F. 2018. The influenza virus hemagglutinin head evolves faster than the stalk domain. *Sci Rep* 8:10432. <https://doi.org/10.1038/s41598-018-28706-1>.
62. Jo S, Kawaguchi A, Takizawa N, Morikawa Y, Momose F, Nagata K. 2010. Involvement of vesicular trafficking system in membrane targeting of the progeny influenza virus genome. *Microbes Infect* 12:1079–1084. <https://doi.org/10.1016/j.micinf.2010.06.011>.
63. Schindelin J, Arganda-Carreras I, Frise E, Kaynig V, Longair M, Pietzsch T, Preibisch S, Rueden C, Saalfeld S, Schmid B, Tinevez JY, White DJ, Hartenstein V, Eliceiri K, Tomancak P, Cardona A. 2012. Fiji: an open-source platform for biological-image analysis. *Nat Methods* 9:676–682. <https://doi.org/10.1038/nmeth.2019>.
64. Kumakura M, Kawaguchi A, Nagata K. 2015. Actin-myosin network is required for proper assembly of influenza virus particles. *Virology* 476:141–150. <https://doi.org/10.1016/j.virol.2014.12.016>.
65. Sugita Y, Noda T, Sagara H, Kawaoka Y. 2011. Ultracentrifugation deforms unfixed influenza A virions. *J Gen Virol* 92:2485–2493. <https://doi.org/10.1099/vir.0.036715-0>.
66. Suzuki Y, Sakai N, Yoshida A, Uekusa Y, Yagi A, Imaoka Y, Ito S, Karaki K, Takeyasu K. 2013. High-speed atomic force microscopy combined with inverted optical microscopy for studying cellular events. *Sci Rep* 3:2131. <https://doi.org/10.1038/srep02131>.
67. Yoshida A, Sakai N, Uekusa Y, Imaoka Y, Itagaki Y, Suzuki Y, Yoshimura SH. 2018. Morphological changes of plasma membrane and protein assembly

- during clathrin-mediated endocytosis. *PLoS Biol* 16:e2004786. <https://doi.org/10.1371/journal.pbio.2004786>.
68. Ichinohe T, Kawaguchi A, Tamura S, Takahashi H, Sawa H, Ninomiya A, Imai M, Itamura S, Odagiri T, Tashiro M, Chiba J, Sata T, Kurata T, Hasegawa H. 2007. Intranasal immunization with H5N1 vaccine plus poly I:poly C12U, a Toll-like receptor agonist, protects mice against homologous and heterologous virus challenge. *Microbes Infect* 9:1333–1340. <https://doi.org/10.1016/j.micinf.2007.06.007>.
69. Kuroki T, Lee S, Hirohama M, Taku T, Kumakura M, Haruyama T, Nagata K, Kawaguchi A. 2018. Inhibition of influenza virus infection by *Lentinus edodes* mycelia extract through its direct action and immunopotentiating activity. *Front Microbiol* 9:1164. <https://doi.org/10.3389/fmicb.2018.01164>.